

Photo-Induced Electron Transfer Reactivity at Nanoscale Semiconductor–Solution Interfaces: Case Studies with Dye-Sensitized SnO₂–Water Interfaces

Dennis A. Gaal and Joseph T. Hupp

Northwestern University, Evanston, Illinois, U.S.A.

I. INTRODUCTION

One of the most exciting and technologically promising areas of application of contemporary photochemistry is the liquid-junction solar cell. Perhaps the most compelling version of the cell is the “Grätzel cell”—a photovoltaic cell that converts sunlight into electricity with nearly 100% quantum efficiency and greater than 10% overall energy efficiency [1–3]. The cell uses a broadly absorbing coordination compound to sensitize a wide-bandgap semiconductor—a high-area nanocrystalline form of TiO₂—to visible light. As shown schematically in Fig. 1, sensitization involves molecular photoexcited-state formation, followed by transfer of an electron (“injection”) from the excited molecule into the conduction band of the semiconductor. The oxidized dye is restored to its chromophoric form by reduction with iodide ions present in the surrounding solution. The electrochemical circuit is completed at a dark electrode, which supplies the electrons needed to regenerate iodide from triiodide.

From the diagram, cell operation comprises a series of interfacial electron-transfer (ET) reactions that yields no net photochemistry—only conversion of

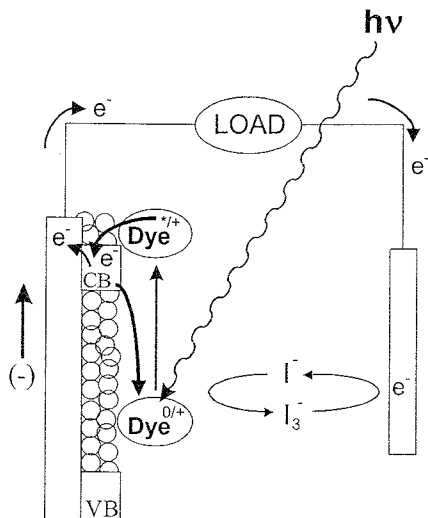


Figure 1 Schematic representation of a Grätzel solar cell. Sub-band-gap light absorption leads to the formation of the sensitizer excited state, followed by electron injection into the conduction band of the high-area nanocrystalline semiconductor. The electrons can be drawn into a circuit to do useful work and returned to the system through the redox mediator, the I/I_3^- couple, at the counterelectrode.

solar energy to heat and electrical energy. In addition, for each of the ET reactions in the light-to-electricity conversion sequence, an energy-wasting back reaction can occur. Clearly, one of the requisites for efficient cell operation is the overall occurrence of comparatively fast forward-ET reactions [4–7] and comparatively slow back-ET processes, such that branching ratios strongly favor the electrical-energy-producing forward sequence. That Grätzel-type cells do this well is evidenced by their near-unity quantum efficiencies [8,9].

We have been especially interested in one particular interfacial ET reaction: back ET from the semiconductor to the dye molecule. Beyond its relevance to solar cell operation [10,11], the reaction is interesting from a fundamental perspective. By monitoring it spectroscopically, one can access interfacial ET kinetics and dynamics at much higher driving forces and on much shorter time scales than generally obtainable by direct electrochemical methods. This, in principle, permits a broader evaluation of factors potentially capable of controlling interfacial redox reactivity—familiar factors such as Marcus-type reorganization energies, surface electronic states, and molecule–surface electronic coupling energies, but also other, less familiar structural and chemical factors. Although the Grätzel

cell is based on titanium dioxide, we have focused—for experimental reasons—on a closely related electrode material, tin oxide (SnO_2), in much of the work described here. Also, for experimental reasons, we have focused on reactions in aqueous environments. The story is almost certainly different in the nonaqueous environments favored for Grätzel-type solar cells, as evidenced especially by recent reports from Meyer [12,13], Lewis [14,15], and their co-workers, among others [16–18].

In the sections that follow, we first outline and summarize, in the context of contemporary ET theory, the experimental behavior of systems involving only weak, electrostatic interactions between dye molecules and the semiconductor surface. This is followed by (1) a description of the behavior of covalently linked dye–semiconductor combinations, which is remarkably different from that seen with weakly interacting systems, (2) a discussion of the fundamental energetics for the reactions—which again appears to differ significantly for the two reaction subclasses—and (3) a comparative discussion of possible interfacial reaction mechanisms.

II. ELECTRON-TRANSFER THEORY

To place experimental studies in context, it is helpful to recall Marcus' semiclassical formulation of ET reaction rate theory. Briefly, for an ET reaction involving weak electronic interactions, the first-order rate constant can be written as [19,20]

$$k_{\text{ET}} = \left(\frac{4\pi^2 H_{\text{ab}}^2}{h} \right) (4\pi\lambda RT)^{-1/2} \exp \left(\frac{-\Delta G^*}{RT} \right) \quad (1)$$

where H_{ab} is the initial-state/final-state electronic coupling energy, h is Planck's constant, λ is the reorganization energy, ΔG^* is the activation free energy, R is the gas constant, and T is temperature. In the classical limit and neglecting any barrier round-off due to H_{ab} , Marcus writes the activation free energy as

$$\Delta G^* = \frac{(\Delta G^\circ + \lambda)^2}{4\lambda} \quad (2)$$

where ΔG° is the free-energy driving force for the reaction. As illustrated in Fig. 2, Eq. 2 yields three reactivity regimes: (1) the normal region ($-\Delta G^\circ < \lambda$), where k_{ET} increases with increasing driving force (more negative ΔG°) and ΔG^* decreases, (2) a barrierless point where $-\Delta G^\circ$ equals λ and k_{ET} reaches its maximum value, and (3) the Marcus inverted region ($-\Delta G^\circ > \lambda$), where k_{ET} decreases with increasing driving force and ΔG^* increases.

III. WEAKLY INTERACTING SYSTEMS

A. Model Systems

Nanoparticulate SnO_2 films and colloids generally feature a slight stoichiometric excess of oxygen and, therefore, a net negative surface charge in water at pHs

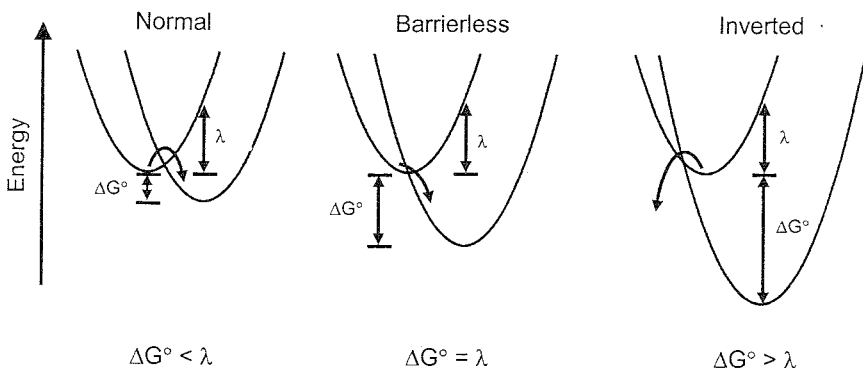
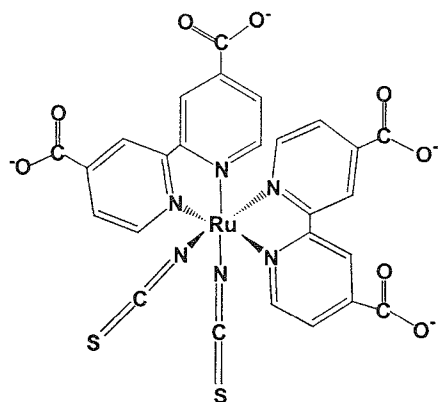


Figure 2 Energy surfaces corresponding to the normal, barrierless, and inverted electron-transfer reactivity regions of Marcus theory.

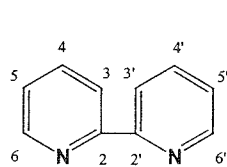
where enough surface oxygen atoms are deprotonated (i.e., pHs greater than 7) [21]. The negative charge can be used to advantage to bind cationic dye molecules via weak electrostatic interactions. The binding turns out to be easier to control if the SnO_2 photoelectrode in Fig. 1 is replaced by colloidal SnO_2 and the reaction sequence is limited to dye injection and back electron transfer. Under these conditions, as Rogers and Ford [22–24] as well as Kamat and co-workers [25–27] have shown, interfacial ET kinetics can be conveniently followed by simple pump/probe-type transient absorbance measurements.

The dyes most often used in the Grätzel cell are polypyridyl complexes of ruthenium, featuring pendant carboxylates for covalent surface attachment [28–30]. The ubiquitous N3 dye (**1**), for example, has the formula $\text{Ru}^{\text{II}}(4,4'\text{-carboxylate-2,2'-bipyridine})_2(\text{NCS})_2^{4-}$ [31–34]. Sensitization is based on visible-region metal-to-ligand charge-transfer (MLCT) absorption, followed by electron injection from one of the two coordinated bipyridines into the photoelectrode's conduction band. The back reaction entails ET from the semiconductor to the oxidized ruthenium center. With this in mind, we examined a set of about a dozen derivatized dicationic *tris*-2,2'-bipyridine (bpy) (**2**) and 1,10-phenanthroline (phen) (**3**) complexes of ruthenium(II) and osmium(II) as colloidal tin oxide sensitizers [35,36]. The idea was to span a very wide range of back-ET driving forces with systems anticipated to be homologous in terms of reorganization energy. To expand the range of driving forces still further, we also examined a few complexes featuring a pair of 4-pyrrolidinopyridine (4ppy) (**4**) or 1-methylimidazole (m-im) (**5**) ligands in place of one of the chelating ligands.

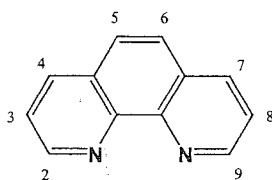


1

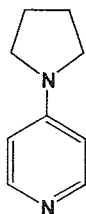
Complex 1



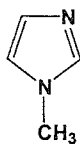
2



3



4



5

Complexes 2–5

B. Preliminary Observations: Dye Sensitivity, Kinetic Heterogeneity, and Reaction Orders

Dye adsorption onto colloidal SnO_2 is accompanied in most cases by essentially complete quenching of dye emission. The simplest interpretation is excited-state consumption via rapid electron injection—a suggestion supported by comparative studies with SiO_2 (an insulator incapable of accepting electrons) in place of SnO_2 and confirmed, for several dyes, by measuring product spectra.

Figure 3 shows representative single-wavelength absorbance transients for three dyes electrostatically bound to colloidal SnO_2 . The transients correspond to photoinitiated bleaching and recovery of the respective MLCT absorbances. From Fig. 3, it is clear that (1) injection is rapid in comparison to back ET, (2) back ET is complex kinetically, but (3) the complex recovery rates depend strongly on the identity of the dye, at least in the first few hundred nanoseconds of the recovery. In order to isolate the shorter-time recovery kinetics, transients were fit, somewhat pragmatically, to a bi-exponential decay function:

$$\Delta A = \Delta A_0 [d \exp(-k_{1,\text{app}}t) + b \exp(-k_{2,\text{app}}t)] + \text{constant} \quad (3)$$

where A is absorbance and ΔA_0 is the change in absorbance just after photoexcita-

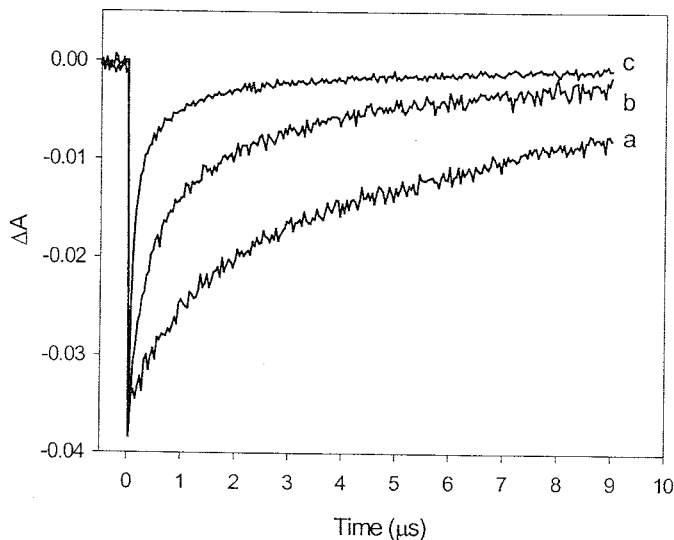


Figure 3 Transient absorbance spectra obtained at the respective MLCT maximum for aqueous SnO_2 colloid sensitized with (a) $\text{Ru}(5\text{-Cl-phen})_3^{2+}$, (b) $\text{Ru}(\text{phen})_3^{2+}$, and (c) $\text{Os}(\text{phen})_3^{2+}$. (Adapted from Ref. 36.)

tion. Similar complexity is routinely encountered for back-ET reactions involving TiO_2 . There it has typically been ascribed to surface-state mediation of the recovery kinetics, where the rate-limiting step can either be interfacial ET from any of several states of differing energy or site-to-site electron hopping on the semiconductor surface prior to interfacial ET, or some combination of the two processes [37–39].

Focusing on the shorter time-scale component, the characteristic recovery time shows a strong dependence on the pump-laser power or, equivalently, the number of electrons injected: The higher the power, the shorter the recovery time. Similar behavior has been noted by Ford et al. [40]. If $k_{1,\text{app}}$ is plotted versus the number of electrons injected per particle (Fig. 4), a linear correlation is obtained. In other words, the reaction appears to be first order in electrons (and first order in the oxidized dye). What does this mean mechanistically? The simplest interpretation—sketched in Scheme 1—is that the injected electrons are free to return to any available dye molecule, not just the molecule from which they originated. This would be the case if injected electrons avoided surface states (at least at these shorter times) and remained in the conduction band. (Notably, the power-dependent kinetic behavior persists in a rigid glass matrix. Consequently, possible

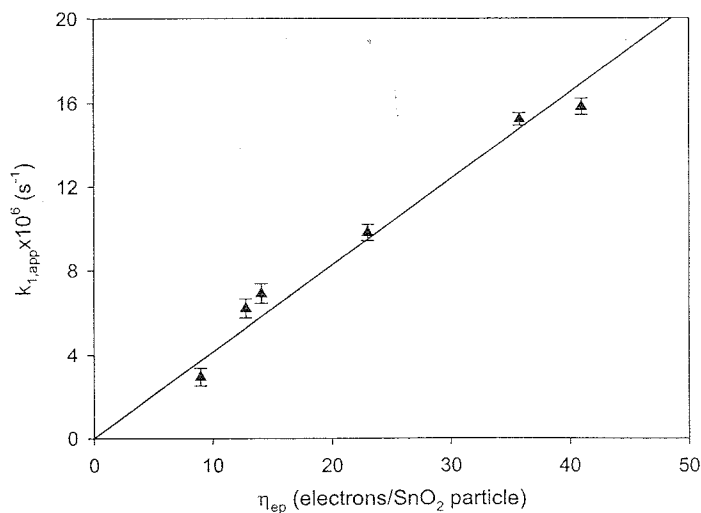
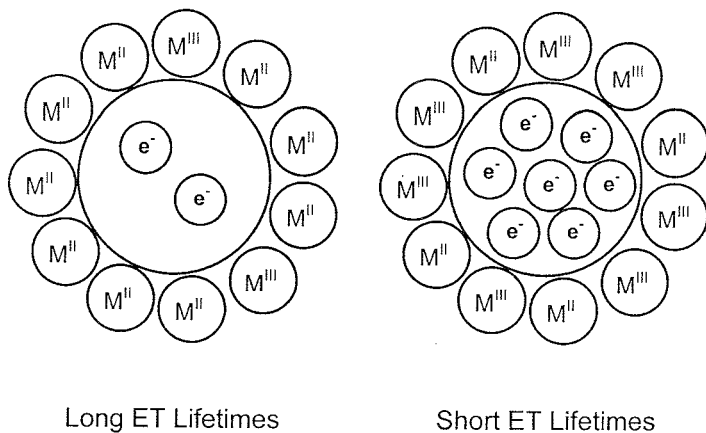


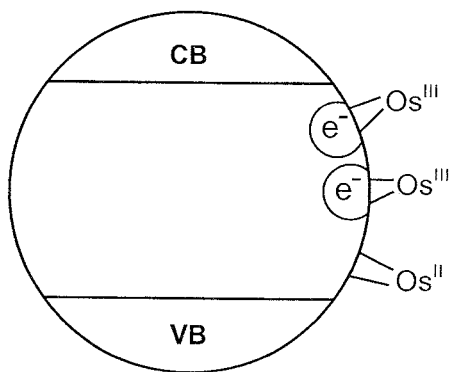
Figure 4 Plot of $k_{1,\text{app}}$ for back ET to Os(phen)_3^{3+} versus η_{ep} , the number of electrons injected per colloidal SnO_2 particle. Note that Eq. (4) contains η_e , the number of electrons injected per unit volume. The estimated average volume for one particle is 1800 nm^3 . (Adapted from Ref. 36.)



Scheme 1

alternative explanations centering on injection-induced dye desorption and subsequent diffusive recovery can be excluded [35].)

In contrast, geminate recombination, caused, for example, by proximal trapping of the injected electron, would yield power-independent recovery times; see Scheme 2. (Of course, if the trapped electrons were not immobilized, but instead were able to migrate rapidly from surface state to surface state, overall second-order behavior would be recovered [37].)



Scheme 2

The second-order kinetics problem for semiconductor–solution interfaces has been considered in some detail by Lewis and co-workers [41,42]. For molecules immobilized on a semiconductor surface and assuming that electrons are transferred from the conduction band, not surface states, their rate law can be written as

$$\text{Rate} = \frac{d[\text{M}^{\text{III}}\text{L}_3^{2+}]}{dt} = k_{1,\text{app}}\Gamma(\text{M}^{\text{III}}\text{L}_3^{3+}) = k_{\text{bET}}\eta_e\Gamma(\text{M}^{\text{III}}\text{L}_3^{3+}) \quad (4)$$

where $\Gamma(\text{M}^{\text{III}}\text{L}_3^{3+})$ is the surface concentration of oxidized dye (mol/cm^2) and η_e is the concentration of electrons in the semiconductor. In this formulation, the units of k_{bET} are cm^3/s , as expected for a second-order interfacial process. The rate constant can be obtained in an approximate way from the slopes of best fit lines of plots of $k_{1,\text{app}}$ versus η_e , constrained to pass through the origin (Fig. 4). A better approach, however, is to refit absorbance transients directly to second-order decays. This procedure yields k_{bET} values that are typically slightly smaller—at most, a factor of 2.

C. Driving-Force Effects

Marcus theory promises that electron-transfer rates will systematically change as ΔG° is changed. For back-ET reactions at the semiconductor–solution interface, ΔG° equals the difference quantity, $E_{\text{cb}} - E_f$, where E_{cb} is the electrochemical potential of the conduction-band edge and E_f is the dye's ground-state formal potential [here, the Ru(III/II) or Os(III/II) couple; see Table 1 for values]. Because the colloidal SnO_2 particles are large enough (~ 15 nm in diameter) for quantum confinement effects to be neglected, E_{cb} for the particles has been equated with E_{cb} for macroscopic tin oxide electrodes (-0.88 versus saturated calomel electrode (SCE) at pH 9) [22].

Figure 5 shows that back-ET rates indeed are sensitive to the driving force, with the log k_{bET} versus ΔG° mapping out a classical Marcus curve that extends significantly into the inverted region. The slight deviations at high driving force have been tentatively ascribed to the participation of a high-frequency vibrational or librational mode. The maximum in the rate plot corresponds to the driving force where the reaction is barrierless and $-\Delta G^\circ$ equals λ . From the plot, λ is ~ 1.4 eV. This value is roughly twice as large as found by Lewis and co-workers in a study of N3-type dyes on titanium dioxide electrodes in acetonitrile as solvent [14] and considerably larger than expected from available estimates of internal and solvent reorganization energies. For example, Brown and Sutin [43] report a kinetically derived reorganization energy of ~ 0.8 eV for the $\text{RuL}_3^{3+}/\text{RuL}_3^{2+}$ self-exchange in homogeneous solution. Also, x-ray crystallographic studies of a related redox pair, $\text{Fe}(\text{phen})_3^{3+}/\text{Fe}(\text{phen})_3^{2+}$, indicate no detectable difference in the M(III)—N versus M(II)—N bond lengths [44] and, therefore, little internal reorganization energy. The solvent contribution (λ_s) to the reorganization energy

Table 1 Electrochemical Data, Driving-Force Information, and Electron-Transfer Values for All Ru and Os Sensitizers

Compound	E_f (V, vs. SCE)	ΔG_{DET} (eV) (pH = 9)	$k_{\text{DET}} \times 10^{13}$ (cm ³ /s)	ΔH^* (kJ/mol)
Ru(5-Cl-phen) ₃ ²⁺	1.39 ^a	-2.27	0.8	20
Ru(phen) ₃ ²⁺	1.27 ^a	-2.15	1.7	14
Ru(bpy) ₃ ²⁺	1.29 ^a	-2.17	1.7	16
Ru(5-CH ₃ -phen) ₃ ²⁺	1.26 ^a	-2.14	1.8	13
Ru(5,6-CH ₃ -phen) ₃ ²⁺	1.23 ^a	-2.11	1.7	13
Ru(4,7-CH ₃ -phen) ₃ ²⁺	1.12 ^a	-2.00	3.0	12
Ru(3,4,7,8-CH ₃ -phen) ₃ ²⁺	1.05 ^a	-1.93	6.8	10
Os(5-Cl-phen) ₃ ²⁺	0.90 ^b	-1.78	5.1	8.6
Os(phen) ₃ ²⁺	0.80 ^c	-1.68	10	7.2
Os(4-CH ₃ -phen) ₃ ²⁺	0.79 ^c	-1.67	12	6.4
Os(4,7-CH ₃ -phen) ₃ ²⁺	0.62 ^c	-1.50	14	7.2
Os(3,4,7,8-CH ₃ -phen) ₃ ²⁺	0.57 ^b	-1.45	15	4.0
Os(phen) ₂ (4py) ₂ ²⁺	0.52 ^c	-1.40	17	5.7
Os(phen) ₂ (m-im) ₂ ²⁺	0.46 ^c	-1.34	13	6.4
Os(4,7-CH ₃ -phen) ₂ (4py) ₂ ²⁺	0.41 ^c	-1.29	16	5.7
Os(4,7-CH ₃ -phen) ₂ (m-im) ₂ ²⁺	0.38 ^c	-1.26	12	11
Os(3,4,7,8-CH ₃ -phen) ₂ (4py) ₂ ²⁺	0.35 ^c	-1.23	13	6.9
Os(3,4,7,8-CH ₃ -phen) ₂ (m-im) ₂ ²⁺	0.31 ^c	-1.19	11	12

^a Juris, A.; Balzani, V.; Barigelletti, F.; Campagna, S.; Belser, P.; Von Zelewsky, A. *Coord. Chem. Rev.* **1998**, *84*, 85–277.

^b Leidner, C. R.; Murray, R. V. *J. Am. Chem. Soc.* **1984**, *106*, 1606–1614.

^c Experimentally measured and corrected from Ag/AgCl to SCE.

can be estimated using continuum theory for a sensitizer at a semiconductor interface as [14,45]

$$\lambda_s = \frac{(\Delta e)^2}{8\pi\epsilon_0} \left[\frac{2}{d} \left(\frac{1}{n^2} - \frac{1}{\epsilon} \right) - \frac{1}{2r} \left(\frac{n_{\text{sc}}^2 - n^2}{n_{\text{sc}}^2 + n^2} \frac{1}{n^2} - \frac{\epsilon_{\text{sc}} - \epsilon}{\epsilon_{\text{sc}} + \epsilon} \frac{1}{\epsilon} \right) \right] \quad (5)$$

where Δe is the amount of charge transferred, n_{sc} and ϵ_{sc} are the refractive index and dielectric constant of the semiconductor, respectively, n and ϵ are the corresponding parameters for the solvent, d is the diameter of the molecule, and r is the separation distance between the sensitizer and the surface. Application of the equation to the tin oxide reactions yields a solvent reorganizational contribution of just 0.3–0.6 eV, leaving roughly 1 eV of reorganization unaccounted for. One possible explanation is that significant reorganizational demands exist on the semiconductor side of the interface—and, indeed, resonance Raman studies of

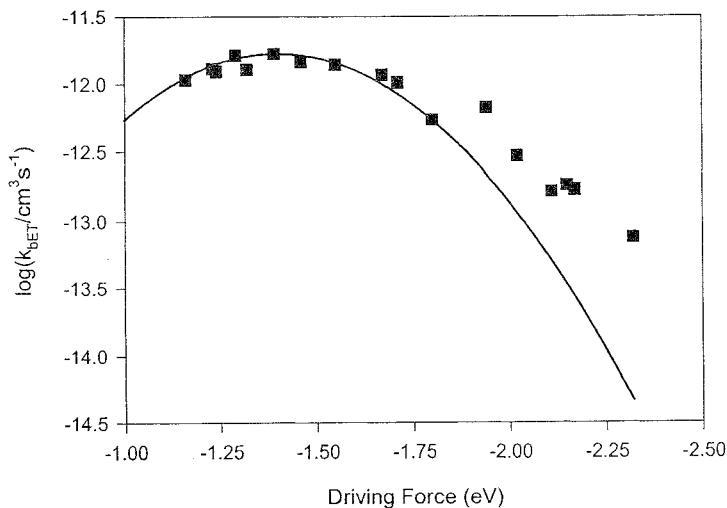


Figure 5 Marcus behavior for the back-ET process at electrostatically sensitized SnO₂ interface for a series of complexes spanning a broad range of redox potentials. Line drawn is a classical Marcus curve [Eq. (1)] based on $\lambda = 1.4$ eV. (Adapted from Ref. 36.)

electron transfer between $\text{Fe}(\text{CN})_6^{4-}$ and titanium dioxide offer one example of such an effect (albeit, with contributions amounting to much less than 1 eV) [46].

D. Photoacoustic Assessment of Reaction Energetics

There is an intriguing alternative explanation for the seemingly exceptionally large reorganization energies: Back ET conceivably could be occurring from trap states having much lower energies than E_{cb} , as sketched in Fig. 6. If so, the true driving force would be less than the difference in energy between the SnO₂ conduction band and the sensitizer redox potential, the ΔG° values in Fig. 5 would be gross overestimates, and the true maximum in the Marcus curve (corresponding to λ) would occur at a much smaller ΔG° .

This idea has been explored via time-resolved interfacial photoacoustic spectroscopy. The method reports on the heat evolved during a reaction [47,48]. Table 2 summarizes results from five back-ET reactions on tin oxide and compares ΔH° values with ΔG° values calculated assuming that electrons are transferred from the conduction band. At short times (corresponding to times used to evaluate $k_{1,\text{app}}$), the agreement is good, validating the Marcus-curve assessment of λ . At longer times (corresponding roughly to times used to evaluate $k_{2,\text{app}}$), ΔH° is about 1 eV less than the conduction-band edge/formal-potential energy

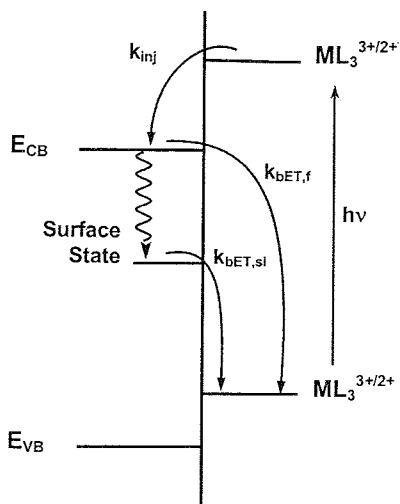


Figure 6 Diagram illustrating qualitative energetics for back ET via two pathways: direct transfer from the bottom of the conduction band and transfer mediated by interfacial surface states (trap states). Note that the rate constants for the two processes may differ.

Table 2 Photoacoustic Energies for Back-ET Reactions at the SnO_2 –Water Interfaces

Compound	$-\Delta G_{\text{DET}}$ (eV) ^a	$-\Delta H'_{\text{DET}}$ (eV) ^b	$-\Delta H^{sl}_{\text{DET}}$ (eV) ^b
$\text{Ru}(\text{phen})_3^{2+}$	2.15	2.4(2)	1.0(2)
$\text{Os}(5\text{-Cl-phen})_3^{2+}$	1.78	1.8(2)	0.6(2)
$\text{Os}(\text{phen})_3^{2+}$	1.68	1.8(2)	0.5(2)
$\text{Os}(4,7\text{-dimethyl-phen})_3^{2+}$	1.50	1.1(3)	<0.3
$\text{Os}(\text{phen})_2(\text{ethylenediamine})^{2+}$	1.41	1.1(3)	ca. 0.2

^a ΔG_{DET} is the back-ET driving force determined from the conduction-band energy and the redox potential of the sensitizer in solution.

^b $\Delta H'_{\text{DET}}$ and $\Delta H^{sl}_{\text{DET}}$ are the thermodynamic reaction enthalpies associated with the fast and slow kinetic components, respectively, determined by photoacoustic spectroscopy.

difference—indicating that under these conditions, back ET occurs from deep traps.

E. Another Look at Driving-Force Effects: pH Effects

Band edges for metal oxide semiconductors, including tin oxide, shift by about -60 mV/pH unit [49,50]. By modulating E_{cb} , pH variations can be used to change ΔG° for back ET in a systematic fashion. Shown in Fig. 7 are pH-dependent rate data reported for two dye couples, $\text{Os}(3,4,7,8\text{-CH}_3\text{-phen})_2(\text{m-im})_2^{3+/2+}$ and $\text{Os}(5\text{-Cl-phen})_3^{3+/2+}$. The back ET rate for the first increases with increasing pH, consistent with its identification as a normal-region reactant in Fig. 5. The second decreases with increasing pH (and increasing driving force), as expected for Marcus inverted-region reactivity. Evidently, pH shifts and formal potential shifts are fully equivalent ways of changing the back-reaction driving force.

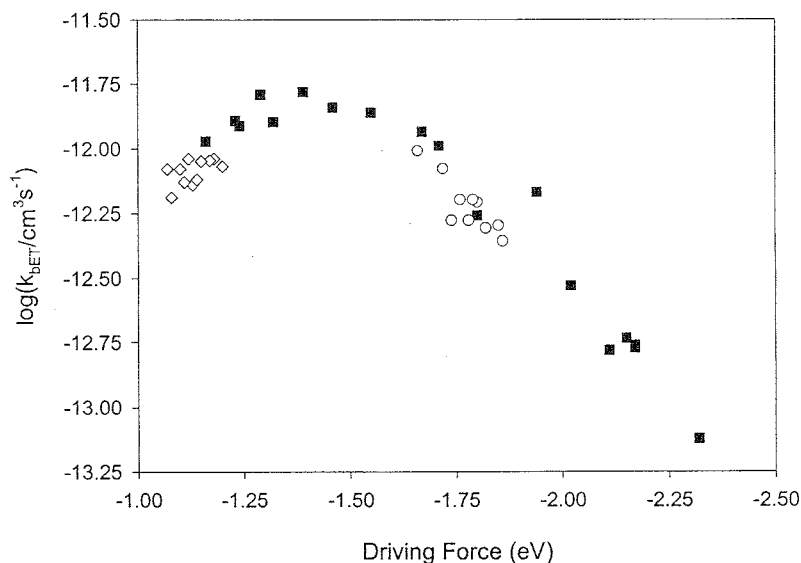


Figure 7 Rate constant versus driving force for the back-ET process at electrostatically sensitized SnO_2 interface for a series of complexes spanning a range of redox potentials. The filled square symbols (■) correspond to data collected at pH=9. Also included in the figure are the results of variable pH studies for $\text{Os}(5\text{-Cl-phen})_3^{3+/2+}$ (◇) and $\text{Os}(3,4,7,8\text{-CH}_3\text{-phen})_2(\text{m-im})_2^{3+/2+}$ (○). The pH variations serve to shift the potential of the conduction band edge. (Adapted from Ref. 36.)

F. Temperature Effects and the Nature of Reorganization Energies

As illustrated by the modified Arrhenius plots in Fig. 8, the back-ET process is thermally activated in both the normal and inverted region, but nearly activationless for reactions occurring at or near the maximum in the rate versus driving-force plot. The findings—especially activation in the inverted region—point to a largely classical reorganizational barrier. Substantive involvement of high-frequency modes would lead to the largely temperature-independent rate behavior usually encountered for inverted kinetics [51,52]. Figure 9 illustrates the mechanistic distinction: Strongly activated behavior implies thermal barrier crossing; temperature-independent or nearly independent behavior implies nuclear tunneling.

Table 1 summarizes the behavior, in the form of activation enthalpies (ΔH^*), for each of 18 reactions. The values listed are somewhat larger than published values [36], reflecting corrections for unrecognized thermal control errors in the original investigation. As expected from classical Marcus theory, decreases in rate are accompanied by increases in ΔH^* . Curiously, however, as the reaction is pushed progressively further into the inverted region, ΔH^* increases by

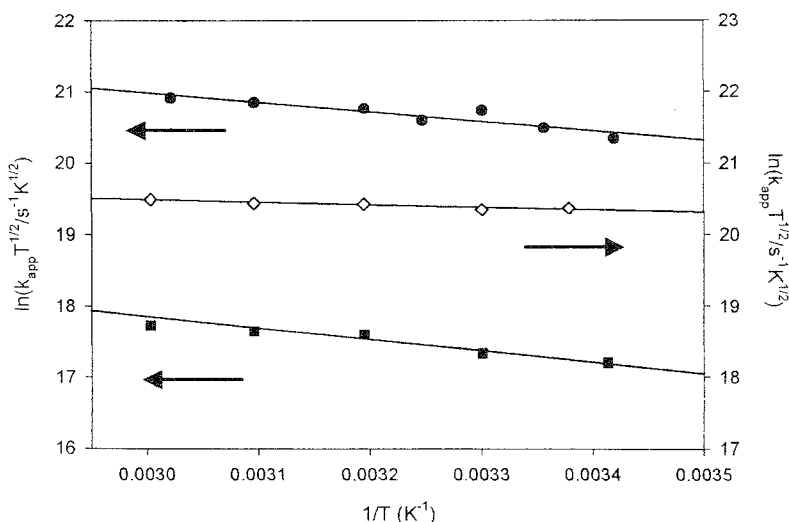


Figure 8 Modified Arrhenius plots for back electron transfer from colloidal SnO_2 to adsorbed Ru(phen)_3^{3+} (■), $\text{Os(3,4,7,8-CH}_3\text{-phen)}_3^{3+}$ (◇), and $\text{Os(3,4,7,8-CH}_3\text{-phen)}_2(\text{m-im})_2^{3+}$ (●). (Adapted from Ref. 36.)

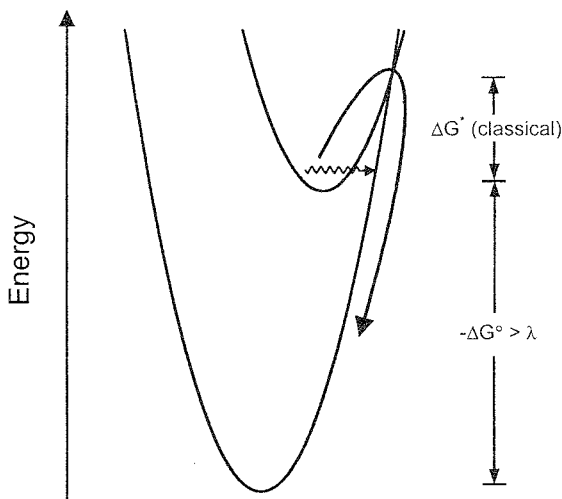


Figure 9 Activated versus tunneling behavior in the Marcus inverted region.

more than the amount needed to accommodate the decreases in rate. Following Marcus and Sutin [53], it has been suggested that the existence of a significant entropic driving force for back ET could account for this peculiar finding [36].

G. Dynamics, Electronic Coupling, and Nonadiabaticity

In addition to providing information about the reorganization energy, rate plots such as Fig. 5 contain quantitative information about dynamics. At the top of the plot, ΔG^* goes to zero and the rate constant can be equated with the pre-exponential part (i.e., the dynamics part) of the applicable classical or semiclassical expression. Under nonadiabatic conditions, Eq.(1) is applicable and, in principle, the initial-state/final-state electronic coupling energy, H_{ab} , can be determined. With an assumption about the effective electronic coupling length (l_{sc}) between the semiconductor and the adsorbed complexes, application of a modified version of Eq. (1) appropriate for second-order kinetics yields for the three reactions closest to the top of the plot H_{ab} values of 20–50 cm^{-1} for the coupling constant [36]. The values are smaller than the frequencies of potentially Franck–Condon active metal–ligand modes, semiconductor phonon modes, and solvent (water) vibrational modes, as well as the frequency of solvent longitudinal relaxation, suggesting that the reactions, indeed, are weakly nonadiabatic.

Because the magnitude of H_{ab} is highly distance sensitive [54], a further diagnostic for nonadiabaticity is a falloff in reaction rate with increasing semicon-

ductor/redox-center separation distance. The separation distance can be altered by incorporating spacers as substituents on the periphery of a ligand. Experiments of this kind using alkyl groups have yielded the expected rate decreases for back-ET reactions. The findings are summarized in Fig. 10, where k_{bET} is plotted versus the number of carbons comprising the alkyl chain. The observed rate decreases point to decreases in the frequency factor. Variable temperature rate measurements confirm that the rate effects come from changes in pre-exponential factors, not activation barriers, and corroborate the conclusion (above) that back ET is nonadiabatic; see Table 3.

Returning to Fig. 10, because the majority of the alkyl groups are flexible and because the interfacial electrostatic binding geometries are unknown, the rate of falloff of k_{bET} or H_{ab}^2 with semiconductor/molecule separation distance cannot be evaluated quantitatively. A curious finding that remains unexplained is that the falloff with osmium complexes is considerably weaker than with ruthenium species. Finally, although the injection reaction was not the focus of the study, spacers clearly do decrease its rate, as shown, for example, by an increase in emission quantum yield (decrease in injection efficiency) with the largest spacers.

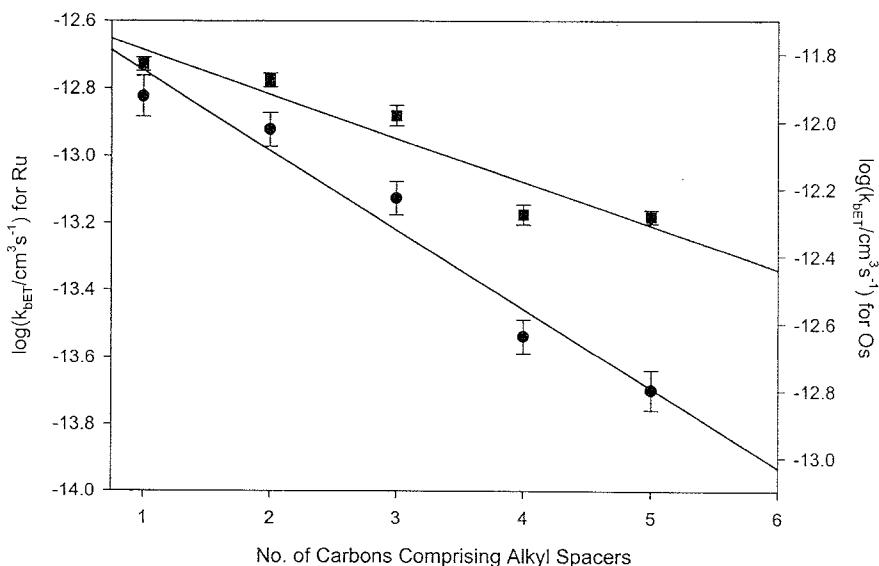


Figure 10 Plot of rate constants for back electron transfer from SnO_2 to electrostatically bound ruthenium (●) and osmium (■) complexes as a function of the number of carbon atoms comprising alkyl spacers. Within experimental error, the driving force for each series of reactions is unaffected by changing the size of the alkyl spacer.

Table 3 Kinetic Parameters for Back Electron Transfer from Colloidal SnO₂ to Several Dyes Featuring Peripheral Alkyl "Spacer" Groups

Compound	$k_{\text{BET}} \times 10^{13} \text{ (cm}^3\text{/s)}$	$\Delta H^* \text{ (kJ/mol)}$
Ru(4,4'-dimethyl-bpy) ₃ ²⁺	1.5(2)	14
Ru(4,4'-diethyl-bpy) ₃ ²⁺	1.2(1)	14
Ru(4,4'-dipropyl-bpy) ₃ ²⁺	0.7(1)	14
Ru(4,4'-dibutyl-bpy) ₃ ²⁺	0.3(1)	15
Ru(4,4'-dipentyl-bpy) ₃ ²⁺	0.2(1)	14
Ru(4,4'-di- <i>t</i> -butyl-bpy) ₃ ²⁺	0.4(1)	15
Os(4,4'-dimethyl-bpy) ₃ ²⁺	14(1)	7.7
Os(4,4'-diethyl-bpy) ₃ ²⁺	13(1)	8.7
Os(4,4'-dipropyl-bpy) ₃ ²⁺	10(1)	7.8
Os(4,4'-dibutyl-bpy) ₃ ²⁺	5.3(3)	7.2
Os(4,4'-dipentyl-bpy) ₃ ²⁺	5.2(2)	9.2
Os(4,4'-di- <i>t</i> -butyl-bpy) ₃ ²⁺	6.0(3)	7.4

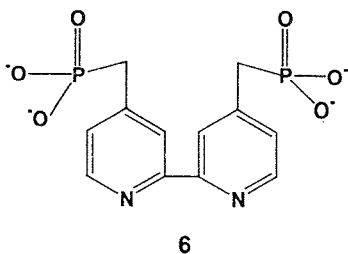
IV. STRONGLY INTERACTING SYSTEMS

A. Surface Attachment Chemistry

Simple electrostatic binding is usually insufficient for long-term dye use in liquid-junction solar cells. Better suited are dyes that are chemically appended to the semiconductor. One approach that works well is carboxylate binding (see N3 dye structure, **1**), either based on esterlike linkages to Ti, Sn, Zr, and so forth or based on interfacial chelation of these atoms [12,55–57]. Even better for certain mechanistic studies, such as rate measurements at elevated temperature or at extreme pHs, are phosphonate linkages. Binding via phosphonate functionalities can be exceptionally robust and extraordinarily persistent [58–62]. By analogy to carboxylates, binding presumably involves either phosphoester linkages to surface metal atoms or phosphonate chelation of the atoms. The available crystallographic literature on Zr(IV) phosphonate compounds supports the phosphoester description [63–65]. In any case, coordination complexes featuring one or more 4,4'-methylphosphonate-2,2'-bipyridine ligands (phosbpy; **6**) have been used to achieve persistent dye attachment to high-area tin oxide photoelectrodes and colloidal particles. As outlined below, the change in mode of binding, although structurally unexceptional, has striking mechanistic consequences.

B. Rate Behavior

Phosphonate attachment of Ru(bpy)₃²⁺ analog to SnO₂ in water as solvent is accompanied by efficient luminescence quenching. Transient absorbance mea-

**Complex 6**

measurements show that the quenching is due to efficient electron injection. In contrast to the behavior of electrostatically bound dyes, the corresponding back-ET reactions exhibit power-independent decay times—in other words, first-order rather than second-order recovery kinetics. (The decays again are complicated, and only the initial portions have been examined in detail.) Similar behavior has been recorded for carboxylated and phosphonated dyes at titanium dioxide–water interfaces [66,67]. The findings have been interpreted in terms of geminate recombination of the injected electron with the oxidized dye, as shown in Scheme 2.

Driving-force studies, using mixed-ligand coordination to alter formal potentials, show only normal-region behavior (Fig. 11), not the inverted Marcus curve seen for electrostatically bound compounds. Similar behavior has been reported for phosphonate-bound dyes on TiO_2 in water [67]. Other studies on TiO_2 in nonaqueous environments have yielded Marcus inverted rate behavior or else no sensitivity to driving force, suggesting that water may induce mechanistically distinct behavior [14,37,68].

As illustrated in Fig. 12, rate measurements as a function of pH or H_0 show almost no change over an extraordinarily wide range—18 pH units (H_0 is the Hammett acidity parameter; it is useful for characterizing proton activities in extremely acidic solutions [69]). The pH range examined corresponds to a change of more than 1.1 eV in E_{cb} and, therefore, ΔG° ! Variations in the back-ET rate by several orders of magnitude would be expected if the behavior paralleled the driving-force dependence summarized in Fig. 11. Again, similar rate behavior has been recorded for phosphonate-bound dyes on titanium dioxide [66]. The origin of the insensitivity to pH-modulated changes in reaction driving force is considered in some detail below.

Variable-temperature studies show that the back reaction is thermally activated. The dependence of ΔH^* on driving force (variations in dye formal potential) is illustrated in Fig. 13 and is consistent with normal-region reactivity [67]. If ΔS^* can be neglected, application of Eq. (1) yields H_{ab} values of approximately

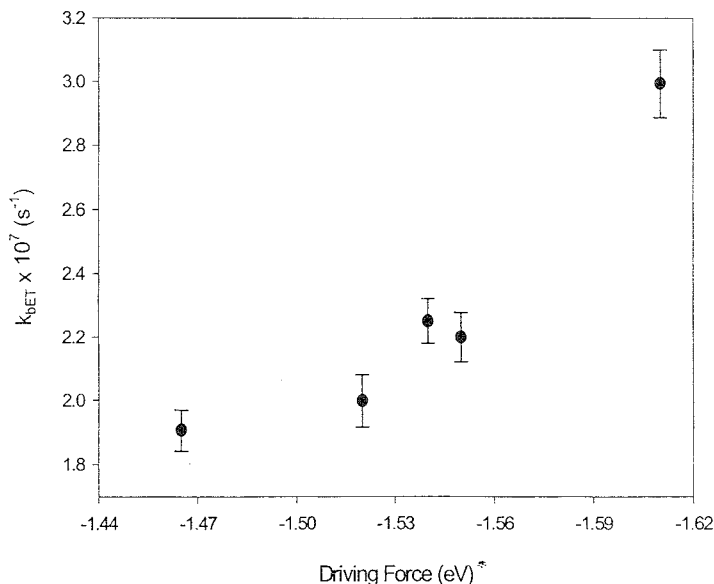


Figure 11 Dependence on driving force of first-order rate constant for back electron transfer from colloidal SnO_2 films to covalently attached complexes. The variations indicate that the reactions occur in the Marcus normal region. The identities of the molecular redox couples, listed from highest driving force to lowest, are, $\text{Ru}^{\text{III/II}}(5\text{-Cl-phen})_2(\text{phosbpy})^{1-/2-}$, $\text{Ru}^{\text{III/II}}(\text{phen})_2(\text{phosbpy})^{1-/2-}$, $\text{Ru}^{\text{III/II}}(4,7\text{-CH}_3\text{-phen})_2(\text{phosbpy})^{1-/2-}$, and $\text{Ru}^{\text{III/II}}(3,4,7,8\text{-CH}_3\text{-phen})_2(\text{phosbpy})^{1-/2-}$.

1 cm^{-1} . These place the reactions in the weakly nonadiabatic regime, implying, therefore, that electronic coupling controls the reaction dynamics. Electronic-coupling-limited rate behavior is consistent with the need to traverse a total of eight bonds in the back reaction, as sketched in Fig. 14. Note that only four bonds are traversed in the injection reaction, suggesting that electronic coupling could be considerably more favorable for this process. Related work has been described by Lian and co-workers for covalently attached dyes on TiO_2 electrodes [70,71].

C. Semiconductor Energetics

The remarkable insensitivity of back-ET rates to pH-induced shifts in the conduction-band edge raises the question of why E_{cb} responds to pH in the first place. Experimentally, conduction-band edges for metal oxide semiconductor electrodes, including SnO_2 electrodes, are observed to shift in the negative direction

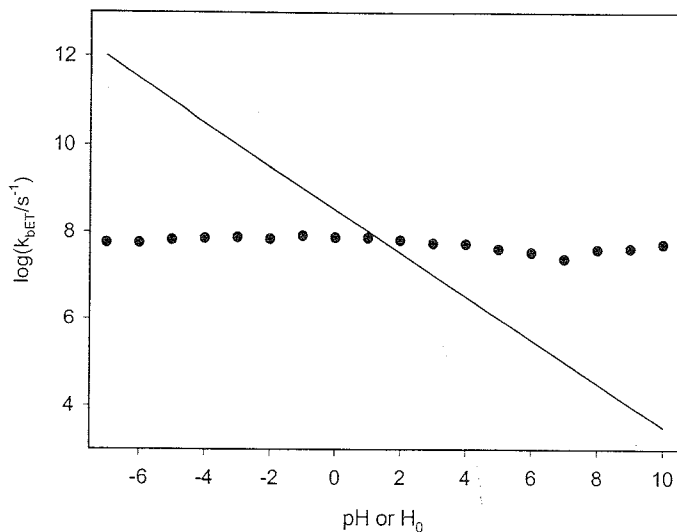


Figure 12 Plot of the first-order rate constant for back ET from high-area SnO_2 electrode to covalently bound $\text{Ru}^{\text{III}}(\text{bpy})_2(\text{phosbpy})^{1-}$ as a function of pH or H_0 . Notably, k_{bET} is nearly pH independent (ca. factor of 3 variations; see Fig. 18). The solid line shows the behavior expected for an inverted reaction based on the 1.1-eV variation in driving force introduced by the pH variations.

by about 60 mV per pH unit [72–78]. The behavior can extend over an enormous pH range: 31 pH units in the case of titanium dioxide, the most extensively examined system [78]. Typical textbook explanations for these “Nernstian shifts” focus on the well-known protonation/deprotonation equilibria of surface oxygen atoms (terminal and bridging oxo and hydroxo groups) [79,80]. The accompanying changes in surface charge induce changes in interfacial potential. The expected form of the interfacial potential versus pH plot, however, is an acid/base titration curve centered at the $\text{p}K_a$ of the surface hydroxo or aquo functionality, not an extended Nernstian shift [81–83]. The surface-protonation explanation actually instead describes the origin of the zeta potential—which does show the expected titration-curve behavior for E versus pH.

Another explanation is that metal oxide electrodes behave like glass pH electrodes. The analogy, however, really does not work: Glass membranes in pH electrodes connect a sample solution with a second, reference solution of known pH. The semiconductor electrode, on the other hand, is in contact with only a single solution.

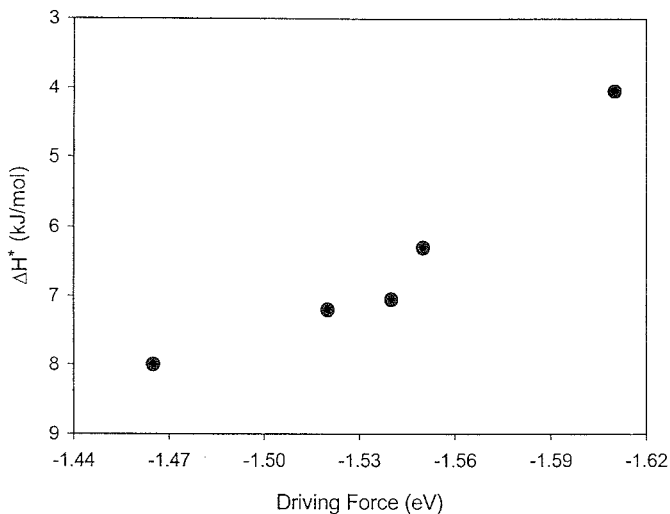


Figure 13 Activation enthalpy for back ET from colloidal SnO_2 films to a series of covalently attached dyes as a function of reaction driving force. See caption to Fig. 11 for identification of the dyes.

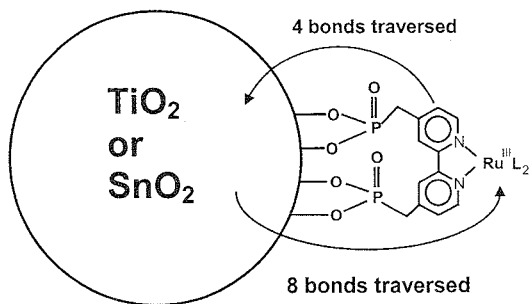
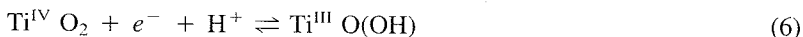


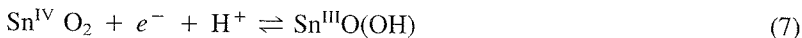
Figure 14 Proposed phosphonate anchoring scheme illustrating the number of bonds traversed in the ligand-based forward reaction (injection reaction) and the metal-ion-based back reaction.

The third explanation, supported by experiment, centers on coupling of proton uptake to electron addition. When the potential of a semiconductor electrode is poised, under dark conditions, at a potential negative of E_{cb} , electrons accumulate near the interface—either in the conduction band or, more typically for nanocrystalline electrodes, in trap states close in energy to E_{cb} [84,85]. Electrochemical quartz-crystal microgravimetry measurements in water with high-area tin oxide, zinc oxide, titanium dioxide, and zirconium dioxide electrodes show that charge-compensating intercalation of cations occurs [49,78,86–90]. With the exception of zinc oxide, which is stable in microgravimetry experiments only at high pHs, the uptake has been shown to occur over a wide range of pHs. Studies with D_2O establish that the species taken up is the proton. Mass comparisons show that even at high pHs, the intercalating species is the proton—indicating that H_2O can serve as the proton source when the concentration of hydronium ions is too low to provide protons. (In nonhydroxylic solvents, electrolyte cations, such as Na^+ and Li^+ are taken up [90,91]—with E_{cb} shifting progressively more negative as the cation size increases and uptake becomes more difficult sterically [92]. In other words, the semiconductor behaves essentially identically to a conventional Li^+ /metal oxide battery electrode) [49,90,93].)

From the Nernst equation, proton-coupled electron addition leads to a -59 mV shift in potential per pH unit. Figure 15 shows the behavior of titanium dioxide and Figure 16 shows the behavior of tin oxide. The plots comprise Pourbaix diagrams for these materials. The breaks observed at extreme pHs with TiO_2 define pK_a 's for $Ti^{IV}O(OH)$ and $Ti^{III}O(OH)$, with the relevant electrochemical equilibrium at less extreme pH or H_0 values [$-8 < pH (H_0) < 23$] described by [78]



The analogous process for tin oxide can be written as



Inorganic chemists generally are unhappy with formulations of tin in oxidation state III. The formulation here ought not to be taken too seriously. Disproportionation into $Sn(IV)$ and $Sn(II)$ conceivably may occur. Alternatively, $Sn^{III}O(OH)$ may well correspond to trapping of an electron by a cluster of tin ions.

D. Driving Forces and Interfacial Thermodynamics

Perhaps the simplest explanation for the pH independence of back-ET rates at metal oxide semiconductor–solution interfaces is that the formal potential of the dye moves in registry with the conduction-band edge. The energy difference, $E_{cb} - E_f$ (dye), is then unchanged with respect to pH and the back-ET reaction experiences a pH-independent driving force. To amplify briefly, the idea is that

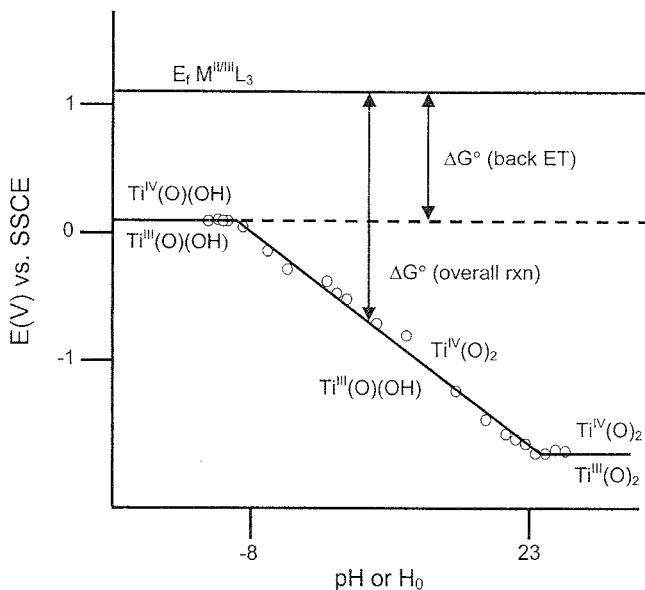


Figure 15 Modified Pourbaix diagram for TiO_2 illustrating the origins of pH-dependent band energetics and the pH-independent back-ET kinetics for covalently anchored dye species. The open circles are experimentally determined values of E_{cb} (combined electrochemical quartz microbalance and reflectance measurements). The driving force for the overall back reaction [coupled electron and proton transfer; cf. Eqs. (10) and (11) for analogous reactions at SnO_2] is pH dependent, but the driving force for the back ET in isolation [cf. Eq. (10)] is pH independent. (Data from Ref. 78.)

a surface-confined redox couple (the dye) will sense the pH-modulated electric field at the interface and the formal potential will be altered accordingly [94,95]. There is good experimental evidence, based on mediator-coupled spectroelectrochemical measurements with TiO_2 , that E_f for some dyes, indeed, can vary with pH—at least in the vicinity of the pH of zero charge (see Chapter 2) [96,97]. As the dye potential shifts, however, matching with the mediator potential becomes less satisfactory and E_f (dye) becomes difficult to determine with good reliability at pHs more than two or three pH units away from the optimal pH for such measurements.

A more broadly applicable approach to evaluating the formal potential of an adsorbed dye is cyclic voltammetry (CV). Under dark conditions, nanocrystalline SnO_2 , TiO_2 , and ZrO_2 electrodes behave as insulators at the potentials needed to oxidize the dyes discussed here. If the dye loading is high, however, the percola-

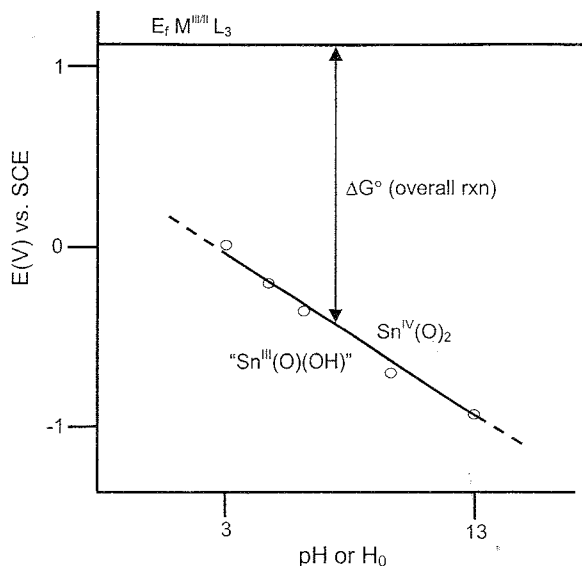


Figure 16 Modified Pourbaix diagram for SnO_2 illustrating the origin of the pH dependence of E_{cb} (see Ref. 73) and showing how the overall back-reaction driving force ($E_{\text{cb}} - E_f$) changes with pH. Insufficient data are available to estimate the driving force for the ET step in isolation (cf. Fig. 15).

tion threshold for charge transport by dye-to-dye electron hopping can be exceeded and CV responses can readily be observed at an underlying conductive platform [98–100]. Because the measurement does not rely upon the conductivity of the photoelectrode, the approach can even be used to measure dye potentials on insulating materials such as alumina.

What do the voltammetry measurements show? Figure 17 is a plot of the formal potential of the $\text{Fe}^{\text{III/II}}(\text{phosbpy})_3^{9-/10-}$ couple on TiO_2 as a function of pH or H_0 between -3 and $+10$. The potentials are reported versus Ag/AgCl at pH 7, but they are corrected for two effects: (1) liquid-junction potentials, which can be significant under conditions of extreme acidity, and (2) protonation of solution-exposed phosphonate substituents. The corrections were done by using a solution-phase redox couple as an internal reference. With the assumption that no more than four of the six available phosphonate groups of the iron complex can bind to the nanocrystalline semiconductor surface, $\text{Ru}^{\text{III/II}}(\text{bpy})_2(\text{phosbpy})^{1-/2-}$ was employed as the internal reference. Figure 17 reveals a sigmoidal variation of E_f with solution pH, but with the variations in E_f confined to pHs close to the pH of zero charge (approximately pH 6) [83,101,102].

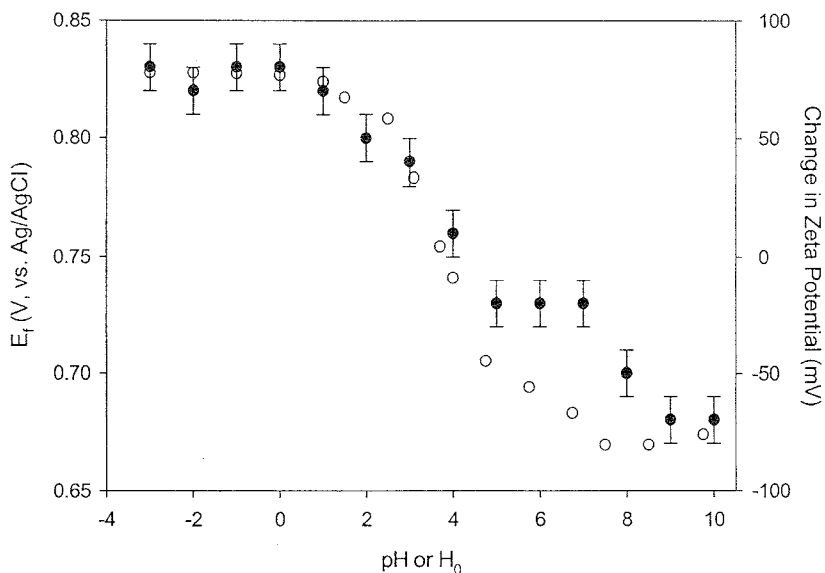


Figure 17 Formal potential of $\text{Fe}^{\text{III/II}}(\text{phosbpy})_3^{9-/10-}$ on nanocrystalline TiO_2 as a function of pH (●), and zeta potentials on TiO_2 function of pH (○). Zeta-potential variations were calculated from electrophoretic transport data contained in Ref. 81. Note the strong correlation between formal potential variations and zeta-potential variations.

If probed over a limited pH range, the sigmoidal dependence could be mistaken for a Nernstian or sub-Nernstian variation of the dye potential with proton activity and a coupling of changes in E_f to changes in E_{cb} . If evaluated over a broader pH range, however, the striking result is not how much E_f changes, but how little. The ~ 180 -mV variation is only a small fraction of the roughly 720 mV change expected if E_f and E_{cb} shifted in tandem. Furthermore, the variations that do occur have the wrong functional form to be explained by a conduction-band coupling effect. Instead, as shown in Fig. 17, the changes in E_f map with very good fidelity onto the changes expected from a simple zeta-potential effect. (This effect is formally analogous to an ion-adsorption-based “effect” upon the apparent formal potential of a surface-confined redox couple at a metal electrode–solution interface [103]. Although not included in the figure, similar behavior is seen for surface-bound $\text{Ru}^{\text{III/II}}(\text{phosbpy})_3^{9-/10-}$, $\text{Os}^{\text{III/II}}(\text{phosbpy})_3^{9-/10-}$, $\text{Ru}^{\text{III/II}}(\text{bpy})_2(\text{phosbpy})^{1-/2-}$, and $\text{Os}^{\text{III/II}}(\text{bpy})_2(\text{phosbpy})^{1-/2-}$ [where the internal reference used for the latter two was the solution-phase $\text{Ru}^{\text{III/II}}(\text{phen})_3^{3+/2+}$ couple].

What about other metal oxide surfaces? The behaviors of the phosphonate-anchored dyes on semiconducting SnO_2 and ZrO_2 and insulating Al_2O_3 surfaces are qualitatively similar (i.e., only weak, non-Nernstian variations of formal potentials with pH are seen). Nevertheless, there are differences. For example, over the investigated range, dye potentials on alumina, in contrast to TiO_2 , do not show the sigmoidal variation with pH. This is consistent with the substantially higher pH of zero charge for alumina ($\text{pH} \sim 9$) [101,104]; shifts in zeta potential, which are responsible for the shifts in E_f on TiO_2 , are unimportant here. For the dyes and surfaces investigated, no evidence for coupling of dye potentials to band-edge potentials is found, and the "coupling" notion can be discarded as an explanation for the approximate pH independence of back-ET rates.

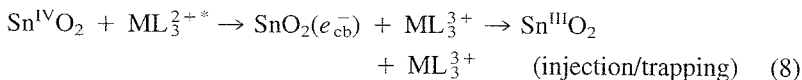
Beyond the extensive studies in aqueous environments, work by Qu and Meyer in acetonitrile as solvent should be noted [12]. Briefly, for dyes immobilized on TiO_2 and ZrO_2 electrodes that had been pretreated in aqueous solutions at pH 1 versus pH 11, they found only minor differences in formal potential—roughly 80 mV—but large differences in E_{cb} .

E. Residual Kinetic Effects

Although back-ET rates for phosphonate-anchored dyes are, for the most part, unaffected by changes in pH, residual effects do exist. Figure 18 presents a more detailed plot of a portion of the rate data contained in Fig. 12. As shown in the figure, modest residual variations in the back-ET rate constant (factor of 3) are paralleled by small variations in the dye potential (-60 mV), where the shapes of both plots are reasonably well described by zeta-potential effects. Assuming that the shifts in E_f translate directly into changes in the free-energy driving force, the combined results are consistent with Marcus normal region behavior (cf. Fig. 11).

F. Mechanistic Interpretations

Any mechanism for back ET for phosphonate-attached dyes must reconcile the seemingly contradictory observations that rates respond to changes in driving force when the changes are introduced by changing the dye's formal potential, but not when they are introduced by changing the conduction-band-edge energy. The mechanism also needs to account for first-order kinetics and for the persistence of normal-region behavior even at very high driving forces. The following sequence [Eqs. (8)–(11)], which parallels a mechanism proposed for back-ET reactions on TiO_2 [67], is consistent with the available data:



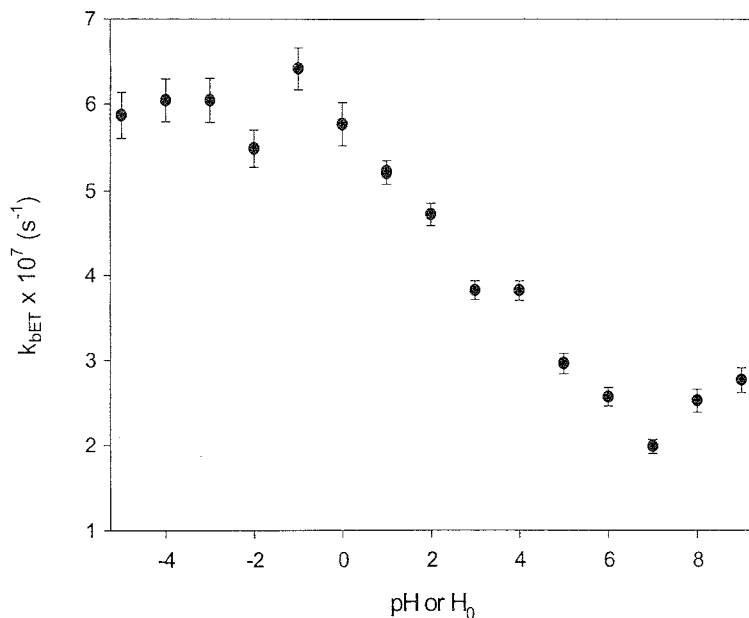
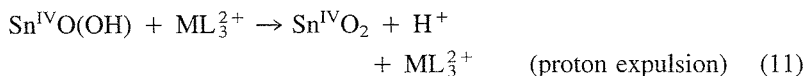
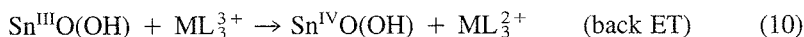
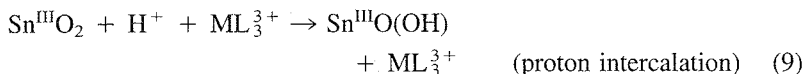


Figure 18 Dependence of back-electron rate constant on pH for $\text{Ru}^{\text{III}}(\text{bpy})_2(\text{phosbpy})^{1-}$ covalently bound to SnO_2 . The observed small reactivity variations (ca. factor of 3) are consistent with a residual zeta-potential-based driving-force effect.



First, injection occurs from the photoexcited dye into the tin oxide conduction band, but is followed by very rapid trapping at a site that is energetically close to the conduction band and physically close to the dye. Trapping is accompanied by rapid, charge-compensating uptake of a proton—either from a hydronium ion or from a water molecule. Perhaps because of the proton uptake, the trapped electron remains proximal to the dye for at least a few hundred nanoseconds. The proximity enables each electron to return precisely to the dye that initially injected it. In other words, the recombination is geminate and the process is first

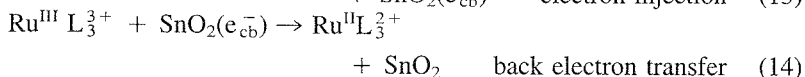
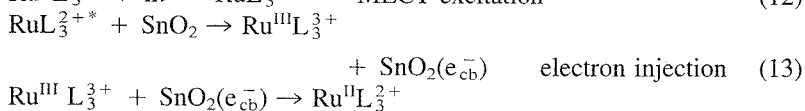
order. Finally, following back ET, the charge-compensating proton is rapidly released by the trap site. The rate-limiting step in this sequence is Eq. (10). Because proton release occurs as a separate, following step, the energy of the electron in this step is governed by the pH-independent $\text{Sn}^{\text{III}}\text{O}(\text{OH})/\text{Sn}^{\text{IV}}\text{O}(\text{OH})$ couple. The band-edge energy, on the other hand, is controlled by the pH-dependent $\text{Sn}^{\text{III}}\text{O}(\text{OH})/\text{Sn}^{\text{IV}}\text{O}_2$ couple. In this scenario, the driving force for the overall back reaction is approximately the difference in energy between E_{cb} and the dye formal potential. This difference increases with increasing pH. The driving force for the rate-determining step, however, is the difference between the pH-independent $\text{Sn}^{\text{III}}\text{O}(\text{OH})/\text{Sn}^{\text{IV}}\text{O}(\text{OH})$ potential and the dye formal potential (also pH independent, apart from small zeta-potential-related perturbations). It is worth noting that similar mechanisms are common in solution-phase photochemistry. For example, the rate of oxidative quenching of $\text{Ru}(\text{bpy})_3^{2+*}$ by anthraquinone disulfonate is pH independent, despite the Nernstian pH dependence of the quinone/hydroquinone formal potential [105]. The rate-limiting step is an isolated electron-transfer step, with proton uptake by the semiquinone occurring in a following step.

Returning to interfacial reactions, the energy diagram in Fig. 15 illustrates, for TiO_2 , how ΔG for the isolated back-ET step differs from ΔG for the overall back reaction (ET + proton expulsion). At typical pHs, the driving force for the isolated back-ET step is considerably smaller than for the overall back reaction. Recognizing the distinction, it is clear, for example, that the kinetically relevant driving forces for back ET from SnO_2 in Fig. 11 are smaller than implied by the figure—meaning that the reorganization energy is similarly smaller.

V. COMPARISONS AND CONCLUSIONS

At least for short to intermediate time scales, the kinetics of back electron transfer at the tin oxide – aqueous solution interface can be described by semiclassical Marcus theory. It follows that interfacial ET, rather than a process such as trap-to-trap electron hopping, must be rate determining for the family of dyes described here. The back-ET reaction is borderline nonadiabatic and is characterized by a surprisingly large reorganization energy. The origin of the large reorganization energy is unclear, but the persistence of thermally activated rate behavior in the Marcus inverted region points to largely classical (i.e., low frequency) contributions.

The detailed mechanism of the back-ET reaction shows a remarkable sensitivity to the mode of binding of the dye to the semiconductor surface. For electrostatically bound dyes, the overall reaction sequence is well described by Eqs. (12)–(14), with back ET evidently occurring directly from the tin oxide conduction band:



For covalently attached dyes, the mechanism is more complex, involving trap states as intermediates and entailing coupled proton transfer. Why do the mechanisms differ? It appears likely that phosphonate- and carboxylate-binding perturb semiconductor surfaces sufficiently to create new trap states that can be rapidly populated following injection. The states are necessarily spatially proximal to the attached dyes, but apparently sufficiently separated from each other to preclude fast trap-to-trap hopping.

If the back ET rate is fast enough, it can attenuate a cell's quantum efficiency. Under certain circumstances (albeit, probably not achieved here), the rate can also influence a cell's photovoltage [10,106,107]. The differing mechanisms for back ET suggest differing criteria for optimization of cell performance under conditions where back ET rates do play a significant role. For example, higher driving forces yield faster rates for normal region reactions (covalently attached reactants), but slower rates for inverted-region reactions (selected electrostatically bound reactants). For polypyridyl-based MLCT chromophores, lower driving forces often go hand in hand with broader spectral coverage. For inverted-region reactions, this implies a trade-off between kinetic optimization (i.e., minimization of back-ET rates) and light collection. For normal-region reactions, on the other hand, kinetic and spectral optimization may well be achievable without a trade-off.

Are the mechanisms described here applicable to cells operating in nonaqueous environments? It is conceivable that the sequence described by Eqs. (12)–(14) occurs under certain conditions. The more complex sequence involving coupled electron and cation transfer probably does not. Although Li^+ (the electrolyte cation most often used in Grätzel-type cells) is known to intercalate into high-area metal oxide semiconductors [49,90,108–111], the rate is probably too slow to be coupled to injection and back ET in the same way that aqueous proton uptake and release are coupled to these processes. The ability to use water itself as a proton source means that solution-phase diffusional limitations on proton uptake are absent. Alkali metal ion uptake from nonaqueous solutions, on the other hand, clearly is subject to diffusional limitations.

The available nonaqueous reactivity data from Meyer and co-workers [13] and from Schmehl and co-workers [60] on injection and back ET to and from TiO_2 appear to point, instead, to a special role for equilibrium cation adsorption. In the absence of initial alkali metal ion adsorption, injection from MLCT-type chromophores does not occur. In their presence, injection does occur, but in

proportion to the amount of cation present. Curiously, the cation concentration appears not to affect rate constants for injection or back ET on TiO_2 —only the yields for these reactions. Presumably, similar behavior would be encountered with SnO_2 electrodes. A speculative interpretation is that alkali metal cation adsorption serves to poise the conduction-band edge of an individual nanoparticle at a potential compatible with exoergic injection. At low cation concentrations, only a fraction of the nanoparticles comprising a high-area photoelectrode may have adsorbed enough cations to permit injection. Obviously, implied in this scheme are local modulation of E_{cb} and a spatially heterogeneous distribution of E_{cb} values under certain conditions.

In summary, at nanostructured tin-oxide semiconductor–aqueous solution interfaces, back ET to molecular dyes is well described by conventional Marcus-type electron-transfer theory. The mechanistic details of the reaction, however, are remarkably sensitive to the nature of the semiconductor–dye binding interactions. The mechanistic differences point, potentially, to differing design strategies for kinetic optimization of the corresponding liquid-junction solar cells.

ACKNOWLEDGMENTS

We gratefully acknowledge the Office of Naval Research for support of this work at the earliest stages and the Basic Energy Science Program of the U.S. Dept. of Energy (grant No. DE-FG02-87ER13808) for subsequent support.

REFERENCES

1. O'Regan, B.; Grätzel, M. *Nature* **1991**, *353*, 737.
2. Bach, U.; Lupo, D.; Comte, P.; Moser, J. E.; Weissörtel, F.; Salbeck, J.; Spreitzer, H.; Grätzel, M. *Nature* **1998**, *398*, 583.
3. Hagfeldt, A.; Grätzel, M. *Acc. Chem. Res.* **2000**, *33*, 269.
4. Hannappel, T.; Burfeindt, B.; Storck, W.; Willig, F. *J. Phys. Chem. B* **1997**, *101*, 6799.
5. Ellingson, R. J.; Asbury, J. B.; Ferrere, S.; Ghosh, H. N.; Sprague, J. R.; Lian, T. Q.; Nozik, A. J. *J. Phys. Chem. B* **1998**, *102*, 6455.
6. Tachibana, Y.; Moser, J. E.; Grätzel, M.; Klug, D. R.; Durrant, J. R. *J. Phys. Chem.* **1996**, *100*, 20,056.
7. Benko, G.; Kallioinen, J.; Korppi-Tommola, J. E. I.; Yartsev, A. P.; Sundstrom, V. *J. Am. Chem. Soc.* **2002**, *124*, 489.
8. Grätzel, M. *Prog. Photovolt.* **2000**, *8*, 171.
9. Parkinson, B. A.; Spitler, M. T. *Electrochim. Acta* **1992**, *37*, 943.
10. Argazzi, R.; Bignozzi, C. A.; Heimer, T. A.; Castellano, F. N.; Meyer, G. J. *J. Phys. Chem. B* **1997**, *101*, 2591.
11. Bonhôte, P.; Moser, J.; Humphrey-Baker, R.; Vlachopoulos, N.; Zakeeruddin, S. M.; Walder, L.; Grätzel, M. *J. Am. Chem. Soc.* **1999**, *121*, 1324.

12. Qu, P.; Meyer, G. J. *Langmuir* **2001**, *17*, 6720.
13. Kelly, C. A.; Farzad, F.; Thompson, D. A.; Stipkala, J. M.; Meyer, G. J. *Langmuir* **1999**, *15*, 7047.
14. Kuciauskas, D.; Freund, M. S.; Gray, H. B.; Winkler, J. R.; Lewis, N. S. *J. Phys. Chem. B* **2001**, *105*, 392.
15. Sauve, G.; Cass, M. E.; Coia, G.; Doig, S. J.; Lauermann, I.; Pomykal, K. E.; Lewis, N. S. *J. Phys. Chem. B* **2000**, *104*, 6821.
16. Haque, S. A.; Tachibana, Y.; Willis, R. L.; Moser, J. E.; Grätzel, M.; Klug, D. A.; Durrant, J. R. *J. Phys. Chem. B* **2000**, *104*, 538.
17. Kamat, P. V.; Bedja, I.; Hotchandani, S.; Patterson, L. K. *J. Phys. Chem.* **1996**, *100*, 4900.
18. Bauer, C.; Boschloo, G.; Mukhtar, E.; Hagfeldt, A. *J. Phys. Chem. B* **2001**, *105*, 5585.
19. Marcus, R. A. *J. Chem. Phys.* **1965**, *43*, 679.
20. Sutin, N. *Adv. Chem. Phys.* **1999**, *106*, 7.
21. Mulvaney, P.; Grieser, F.; Meisel, D. *Langmuir* **1990**, *6*, 567.
22. Ford, W. E.; Rodgers, M. A. J. *J. Phys. Chem.* **1994**, *98*, 3822.
23. Ford, W. E.; Rodgers, M. A. J. *J. Phys. Chem.* **1994**, *98*, 7415.
24. Ford, W. E.; Rodgers, M. A. J. *J. Phys. Chem. B* **1997**, *101*, 930.
25. Barazzouk, S.; Lee, H.; Hotchandani, S.; Kamat, P. V. *J. Phys. Chem. B* **2000**, *104*, 3616.
26. Martini, I.; Hartland, G. V.; Kamat, P. V. *J. Phys. Chem. B* **1997**, *101*, 4826.
27. Nasr, C.; Liu, D.; Hotchandani, S.; Kamat, P. V. *J. Phys. Chem.* **1996**, *100*, 11,054.
28. Hara, K.; Sugihara, H.; Tachibana, Y.; Ashraful, I.; Yanagida, M.; Sayama, K.; Arakawa, H. *Langmuir* **2001**, *17*, 7280.
29. Zakeeruddin, S. M.; Nazeeruddin, M. K.; Humphry-Baker, R.; Pechy, P.; Quagliotto, P.; Barolo, C.; Viscardi, G.; Grätzel, M. *Langmuir* **2002**, *18*, 952.
30. Kleverlaan, C. J.; Indelli, M. T.; Bignozzi, C. A.; Pavanin, L.; Scandola, F.; Hasselmann, G. M.; Meyer, G. J. *J. Am. Chem. Soc.* **2000**, *122*, 2840.
31. Nazeeruddin, M. K.; Kay, A.; Rodicio, I.; Humphry-Baker, R.; Muller, E.; Liska, P.; Vlachopoulos, N.; Grätzel, M. *J. Am. Chem. Soc.* **1993**, *115*, 6382.
32. Oskam, G.; Bergeron, B. V.; Meyer, G. J.; Searson, P. C. *J. Phys. Chem. B* **2001**, *105*, 6867.
33. Fillinger, A.; Parkinson, B. A. *J. Electrochem. Soc.* **1999**, *146*, 4559.
34. Kallioinen, J.; Lehtovuori, V.; Myllyperkio, P.; Korppi-Tommola, J. E. I. *Chem. Phys. Lett.* **2001**, *340*, 217.
35. Dang, X. J.; Hupp, J. T. *J. Am. Chem. Soc.* **1999**, *121*, 8399.
36. Gaal, D. A.; Hupp, J. T. *J. Am. Chem. Soc.* **2000**, *122*, 10956.
37. Hasselmann, G. M.; Meyer, G. J. *J. Phys. Chem. B* **1999**, *103*, 7671.
38. Nelson, J.; Haque, S. A.; Klug, D. R.; Durrant, J. R. *Phys. Rev. B* **2001**, *30*, 5321.
39. Tachibana, Y.; Haque, S. A.; Mercer, I. P.; Durrant, J. R.; Klug, D. A. *J. Phys. Chem. B* **2000**, *104*, 1198.
40. Ford, W. E.; Wessels, J. M.; Rodgers, M. A. J. *J. Phys. Chem. B* **1997**, *101*, 7435.
41. Royea, W. J.; Fajardo, A. M.; Lewis, N. S. *J. Phys. Chem. B* **1997**, *101*, 11,152.
42. Lewis, N. S. *Annu. Rev. Phys. Chem.* **1991**, *42*, 543.

43. Brown, G. M.; Sutin, N. *J. Am. Chem. Soc.* **1979**, *101*, 883.
44. Brunschwig, B. S.; Creutz, C.; McCartney, D. H.; Sham, T. K.; Sutin, N. *Faraday Discuss. Chem. Soc.* **1982**, *74*, 113.
45. Marcus, R. A. *J. Phys. Chem. B.* **1991**, *95*, 2010.
46. Blackbourn, R. L.; Johnson, C. S.; Hupp, J. T. *J. Am. Chem. Soc.* **1991**, *113*, 1060.
47. Leytner, S.; Hupp, J. T. *Chem. Phys. Lett.* **2000**, *330* 3–4, 231.
48. Braslavsky, S. E.; Heibel, G. E. *Chem. Rev.* **1992**, *92*, 1381.
49. Lemon, B. I.; Lyon, L. A.; Hupp, J. T. In *Nanoparticles and Nanostructured Films: Preparation, Characterization, and Applications*; Fendler, J. H., Ed., Wiley-VCH: New York, 1998, p. 335.
50. Finklea, H. O., *Semiconducting Electrodes*; Elsevier: New York, 1988.
51. Bixon, M.; Jortner, J. *J. Phys. Chem.* **1991**, *95*, 1941.
52. Moser, J. E.; Grätzel, M. *Chem. Phys.* **1993**, *176*, 493.
53. Marcus, R. A.; Sutin, N. *Biochim. Biophys. Acta* **1985**, *811*, 265.
54. Closs, G. L.; Miller, J. R. *Science*, **1988**, *240*, 440.
55. Lees, A. C.; Kleverlaan, C. J.; Bignozzi, C. A.; Vos, J. G. *Inorg. Chem.* **2001**, *40*, 5343.
56. Finnie, K. S.; Bartlett, J. R.; Woolfrey, J. L. *Langmuir* **1998**, *14*, 2744.
57. Argazzi, R.; Bignozzi, C. A.; Heimer, T. A.; Castellano, F. N.; Meyer, G. J. *Inorg. Chem.* **1994**, *33*, 5741.
58. Gillaizeau-Gauthier, I.; Odobel, F.; Alebbi, M.; Argazzi, R.; Costa, E.; Bignozzi, C. A.; Qu, P.; Meyer, G. J. *Inorg. Chem.* **2001**, *40*, 6073.
59. Yan, S. G.; Lyon, L. A.; Lemon, B. I.; Prieskorn, J. S.; Hupp, J. T. *J. Chem. Educ.* **1997**, *74*, 657.
60. Andersson, A. M.; Isovitsch, R.; Miranda, D.; Wadhwa, S.; Schmehl, R. H. *Chem. Commun.* **2000**, *6*, 505.
61. Ferrere, S. *Chem. Mater.* **2000**, *12*, 1083.
62. Pechy, P.; Rotzinger, F. P.; Nazeeruddin, M. K.; Kohle, O.; Zakeeruddin, S. M.; Humphry-Baker, R.; Grätzel, M. *J. Chem. Soc. Chem. Commun.* **1995**, *1*, 65.
63. Alberti, G. *Acc. Chem. Res.* **1978**, *11*, 163.
64. Clearfield, A.; Smith, G. D. *Inorg. Chem.* **1969**, *8*, 431.
65. Chakraborty, D.; Chandrasekhar, V.; Bhattacharjee, M.; Kratzner, R.; Roesky, H. W.; Noltemeyer, M.; Schmidt, H. G. *Inorg. Chem.* **2000**, *39*, 23.
66. Yan, S. G.; Hupp, J. T. *J. Phys. Chem.* **1996**, *100*, 6867.
67. Yan, S. G.; Prieskorn, J. S.; Kim, Y.; Hupp, J. T. *J. Phys. Chem. B.* **2000**, *104*, 10,871.
68. Martini, I.; Hodak, J. H.; Hartland, G. V. *J. Phys. Chem. B.* **1998**, *102*, 607.
69. Rochester, C. H. *Acidity Functions*; Academic Press: New York, 1970.
70. Asbury, J. B.; Hao, E.; Wang, Y.; Lian, T. Q. *J. Phys. Chem. B.* **2000**, *104*, 11,957.
71. Asbury, J. B.; Hao, E.; Wang, Y.; Ghosh, H. N.; Lian, T. Q. *J. Phys. Chem. B.* **2001**, *105*, 4545.
72. Bedja, I.; Kamat, P. V.; Hua, X.; Lappin, A. G.; Hotchandani, S. *Langmuir* **1997**, *13*, 2398.
73. Bolts, J. M.; Wrighton, M. S. *J. Phys. Chem.* **1976**, *80*, 2641.
74. Watanabe, T.; Fujishima, A.; Tatsuoki, O.; Honda, K. *Bull. Chem. Soc. Japan*, **1976**, *49*, 8.

75. Redmond, G.; O'Keefe, A.; Burgess, C.; MacHale, C.; Fitzmaurice, D. *J. Phys. Chem.* **1993**, *97*, 11,081.
76. Gottesfeld, S.; McIntyre, J. D. E. *J. Electrochem. Soc.* **1979**, *126*, 742.
77. Natan, M. J.; Mallouk, T. E.; Wrighton, M. S. *J. Phys. Chem.* **1987**, *91*, 648.
78. Lyon, L. A.; Hupp, J. T. *J. Phys. Chem. B.* **1999**, *103*, 4623.
79. Kalaysundaram, K.; Grätzel, M.; Pelizetti, E. *Coord. Chem. Rev.* **1986**, *67*, 57.
80. Healy, T. W.; White, L. R. *Adv. Colloid Interf. Sci.* **1978**, *9*, 303.
81. Boxall, C. *Chem. Soc. Rev.* **1994**, *23*, 137.
82. Boxall, C.; Kelsall, G. H. *J. Electroanal. Chem.* **1992**, *328*, 75.
83. Nelson, B. P.; Candal, R.; Corn, R. M.; Anderson, M. A. *Langmuir* **2000**, *1*, 6094.
84. Boschloo, G.; Fitzmaurice, D. *J. Phys. Chem. B.* **1999**, *103*, 7860.
85. Boschloo, G.; Fitzmaurice, D. *J. Electrochem. Soc.* **2000**, *147*, 1117.
86. Lemon, B. I.; Hupp, J. T. *J. Phys. Chem. B.* **1997**, *101*, 2426.
87. Lemon, B. I.; Hupp, J. T. *J. Phys. Chem.* **1996**, *100*, 14,578.
88. Lemon, B. I. Ph.D. dissertation, Northwestern University, Evanston, IL, 1999.
89. Lyon, L. A. Ph. D. dissertation, Northwestern University, Evanston, IL, 1996.
90. Lyon, L. A.; Hupp, J. T. *J. Phys. Chem.* **1995**, *99*, 15,718.
91. Krtil, P.; Kavan, L.; Fattakhova, D. *J. Solid State Electron.* **1997**, *1*, 83.
92. Redmond, G.; Fitzmaurice, D. *J. Phys. Chem.* **1993**, *97*, 1426.
93. Exnar, I.; Kavan, L.; Huang, S. Y.; Grätzel, M. *J. Power Sources* **1997**, *68*, 720.
94. Creager, S. E.; Weber, K. *Langmuir* **1993**, *9*, 844.
95. Smith, C. P.; White, H. S. *Anal. Chem.* **1992**, *64*, 2398.
96. Zaban, A.; Ferrere, S.; Sprague, J.; Gregg, B. A. *J. Phys. Chem. B.* **1997**, *101*, 55.
97. Zaban, A.; Ferrere, S.; Gregg, B. A., *J. Phys. Chem. B.* **1998**, *102*, 452.
98. Bonhôte, P.; Gogniat, E.; Tingry, S.; Barbe, C.; Vlachopoulos, N.; Lenzmann, F.; Comte, P.; Grätzel, M. *J. Phys. Chem. B.* **1998**, *102*, 1498.
99. Heimer, T. A.; D'Arcangelis, S. T.; Farzad, F.; Stupkala, J. M.; Meyer, G. J. *Inorg. Chem.*, **1996**, *35*, 5319.
100. Trammell, S. A.; Meyer, T. J. *J. Phys. Chem. B.* **1999**, *103*, 104.
101. Deo, G.; Wachs, I. E. *J. Phys. Chem.* **1991**, *95*, 5889.
102. Moser, J.; Punchihewa, S.; Infelta, P. P.; Grätzel, M. *Langmuir* **1991**, *7*, 3012.
103. Hupp, J. T.; Weaver, M. J. *J. Electroanal. Chem.* **1983**, *145*, 43.
104. Veeramasuneni, S.; Yalamanchili, M. R.; Miller, J. D. *J. Colloid Interf. Sci.* **1996**, *184*, 594.
105. Darwent, J. R.; Kalyanasundaram, K. *J. Chem. Soc. Faraday Trans.* **1981**, *77*, 373.
106. Cahen, D.; Hodes, G.; Grätzel, M.; Guillemoles, J. F.; Riess, I. *J. Phys. Chem. B.* **2000**, *104*, 2053.
107. van de Lagemaat, J.; Park, N. G.; Frank, A. J. *J. Phys. Chem. B.* **2000**, *104*, 2044.
108. Shouji, E.; Buttry, D. A. *Electrochim. Acta*, **2000**, *45*(22–23), 3757.
109. Guerfi, A.; Paynter, R. W.; Dao, L. H. *J. Electrochem. Soc.* **1995**, *142*, 3457.
110. Chemseddine, A.; Morineau, R.; Livage, J. J. *Solid State Ionics* **1983**, *9–10*, 357.
111. Yu, A. S.; Frech, R. *J. Power Sources*, **2002**, *104*, 97.